Relation-Oriented: Toward Causal Knowledge-Aligned AI

Anonymous authors
Paper under double-blind review

Abstract

This study examines the inherent limitations of the prevailing *Observation-Oriented* learning paradigm by understanding relationship modeling from a unique dimensionality perspective. This paradigm necessitates the identification of modeling objects prior to defining relations, confining models to observational space, and limiting their access to dynamical temporal features. By relying on a singular, absolute timeline, it often neglects the multi-dimensional nature of the temporal feature space. This oversight compromises model robustness and generalizability, contributing significantly to the AI misalignment issue.

Drawing from the relation-centric essence of human cognition, this study presents a new *Relation-Oriented* paradigm, complemented by its methodological counterpart, the *relation-defined representation* learning, supported by extensive efficacy experiments.

1 Introduction

The prevailing modeling paradigm rules that observed variables (and outcomes) are the premise of building relationships. Model variables are often estimated by their observational values with an independent and identical distribution (i.i.d.) setting. Back in the 1890s, Picard-Lindelof theorem introduced a *logical timeline* t to record observational timestamps, establishing the paradigm $x_{t+1} = f(x_t)$ to depict variable X's time evolution. Since then, this ***Observation-Oriented*** principle has become our learning convention, where the temporal dimensionality is equated to the counts of $\{t, t+1\}$ unit, a predetermined constant time lag.

For a relationship $X \to Y$, the model can be in form $y_{t+m} = f(x_t)$, or $y_{t+m} = f(\{x_t\})$, where $\{x_t\} = \{x_1, \ldots, x_t, x_{t+1}, \ldots, x_T\}$ represents a time sequence of X within a certain length T, and a predetermined time progress m from X to Y. No matter in which form, the outcome Y is strictly observational only, leaving all potentially significant temporal changes of Y completely managed by $f(\cdot)$. However, although function $f(\cdot)$ can be selected as *linear* or *nonlinear*, the time evolution from t to $t+m$ is always left as *linear*.

Such a conventional linearity on the temporal dimension may be sufficient in the past, but not present, given the current technological advancements in data collection and Artificial Intelligence (AI) learning. Exploring nonlinear temporal distributions is gradually becoming essential. From a broader viewpoint, this is calling for a new modeling paradigm Scholkopf et al. (2021), which does not rest on the conventional i.i.d. assumed observations, but can treat t as a distinct computational dimension.

This study aims to fundamentally reveal the inherent deficiency of the current *Observation-Oriented* modeling paradigm (Chapter I: Sections 2-4), and accordingly propose the new ***Relation-Oriented*** one as desired, along with feasibility validations (Chapter II: Sections 5-7). Particularly, the single absolute timeline t that we conventionally use, inherently cannot capture the multifaceted nature of temporal dimensionality, leading to widespread biases and resulting in AI models misaligned with our cognitive understanding, contributing significantly to the AI misalignment issue Christian (2020).

In this paper, we approach the concept of relationships in modeling through a novel *dimensionality framework*, offering a unique perspective. The remainder of this section aims to lay the groundwork. Then, in Chapter I, we will inspect causal learning from the view of temporal dimensionality, highlighting the key role of relations in modeling. Subsequently, Chapter II will concentrate on the proposed ***relation-defined representation*** learning method, which embodies the advocated *Relation-Oriented* modeling paradigm.

1.1 Manifestation of AI Misalignment

Today, AI has displayed capabilities surpassing humans in solely observational learning tasks, such as generating images, Go gaming, and so on. However, AI may appear "unintelligent" in comprehending certain relations that humans find intuitive. For instance, AI-created personas on social media can have realistic faces but barely with the presence of hands, due to AI struggling with the complex structure, instead treating hands as arbitrary assortments of finger-like items.

Moreover, when it comes to time evolution, causal reasoning presents a substantial challenge for AI, although it is innate for humans. Traditional causal learning methods, while having made valuable contributions to various fields of knowledge over the years Wood (2015); Vuković (2022); Ombadi et al. (2020), often suffer from a limitation in their generalizability Scholkopf et al. (2021). Unsuccessful neural network applications are particularly evident when addressing large-scale causal questions Luo et al. (2020). As a result, these methods are often confined to context-specific applications and encounter difficulties in extending to diverse scenarios. Thus, it is not strange that AI's capability on the temporal dimension remains notably constrained.

The questions "How to leverage AI's capability in causality" and "How to simulate hands with reasonable fingers" may seemly pertain to specific domains such as causal inference and computer vision. However, they fundamentally converge toward the broader challenge of AI Alignment, encapsulated by the essential question: "*Why are these relations unseen to AI?*" Reflecting on Dr. Geoffrey Hinton's warning, the misalignment of AI capabilities with human values can result in unintended and potentially harmful consequences. It is becoming increasingly critical to address this essential question.

1.2 Relations in Hyper-Dimension

Consider a pairwise relationship comprised of three elements: two *observable* objects, and a relation connecting them, which comes from our knowledge. The two objects can be solely observational (e.g., images, spatial coordinates of a quadrotor, etc.), or either observational-temporal (e.g., trends of stocks, persistent rain for five hours, etc.). Interestingly, the "relation" has to be ***unobservable*** to make this relationship meaningful for machine learning, distinguished from mere statistical dependencies.

This principle was initially introduced in the form of Common Cause Dawid (1979); Scholkopf et al. (2021), suggesting that any nontrivial conditional independence between two observables requires a third, mutual cause (i.e., our *unobservable* "relation"). Take the relationship "Bob has a son named Jim" as an example. The father-son relation is unobservable information that exists in our knowledge, which can also be seen as the common cause that makes their connection unique rather than any random pairing of "Bob" and "Jim". Given sufficient observed social activities, AI may deduce this pair of "Bob" and "Jim" have some special connection, but that does not equate to discerning their genuine father-son relation.

Put simply, the existence of unobservable element(s) makes the relationship model informative. In other words, the information contained by the model stems from our knowledge, rather than direct observations. Let's denote the model as $Y = f(X; \theta)$ with θ indicating the function parameter in demand. Then, in the context of modeling, the term "relation" can be represented by θ.

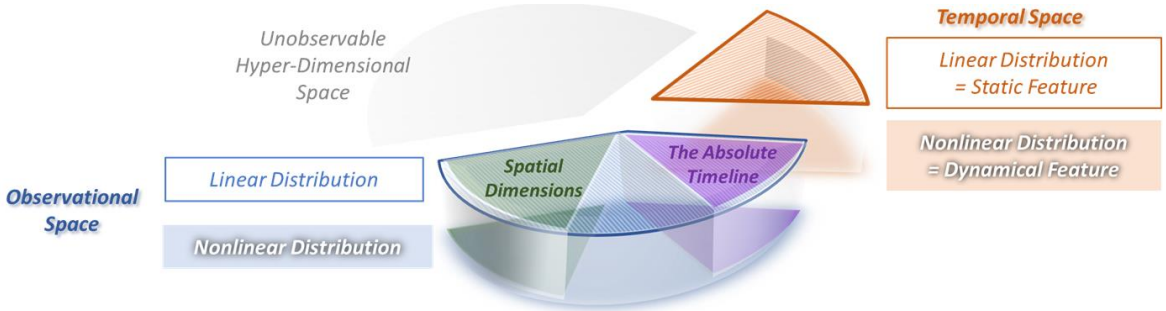

Figure 1: *Observational*, *Temporal*, and *Hyper-Dimensional* spaces, with the former two *Observable*.

From a dimensionality standpoint, a relationship can be viewed as a joint distribution across multiple dimensions: The observable objects feature the distribution on observational-temporal dimensions, while the unobservable relation manifests as some unseen distribution on a hyper-dimension. As illustrated in Figure 1,

our cognitive space storing the knowledge relationships can be divided into three categories accordingly, where the ***Hyper-Dimensional*** space symbolizes the collective of all unobservable relations within our knowledge. Chapter I of this study aims to examine why AI cannot autonomously model certain relations in this space and understand the implications for its learning results.

1.3 Observational and Temporal Spaces

Under the *Observation-Oriented* principle, current models largely operate within the observational space. For example, CNNs (Convolutional Neural Networks) can learn observational associations among two-dimensional pixels; a quadrotor's movement can be estimated in three spatial dimensions; LLMs (Large Language Models) work in a semantic space along a logical timeline representing the order of words. Some applications (e.g., the last two examples) are aligned with the Picard-Lindelof theorem, using a single logical timeline to depict the absolute time evolution, thus often referred to as spatial-temporal analysis Alkon (1988); Turner (1990); Andrienko (2003). However, in a modeling context, an attribute of timestamps is not distinguishable from other observational attributes, unnecessarily to be temporally significant. Thus, we classify this single absolute timeline scenario as within the observational space.

According to our discussions at the beginning, the form of timestamps can only capture *linear* relationships on the temporal dimension, thus fundamentally impeding AI's ability to handle the temporal *nonlinearity*. This inherent disparity between our knowledge understanding and established models results in misalignment (see Section 3.3 for further discussions), accentuated by the rise of highly efficient AI applications.

Moreover, in our cognition (not the modeling context), ***multiple*** *logical timelines* may exist to form the temporal feature space in Figure 1 (see Section 4 for further insights). However, the current modeling paradigm has determined they cannot be distinguished as different dimensions in computation but crudely represented by an attribute of timestamps, i.e., consolidated as a single timeline.

In the observational-temporal joint space, as shown in Figure 1, observable distributions can be categorized as either *linear* or *nonlinear*. The temporal-significant ones can manifest as "static" or "dynamical" temporal features within a modeling context. For example, in the relationship "rain leads to wet floors", the events "rain" and "wet floors" are snapshots at specific timestamps and are thus viewed as ***static*** *temporal* objects. In contrast, events such as "persistent rain for five hours" and "floors becoming progressively wetter" are considered ***dynamical*** *temporal* due to their indispensable sequential patterns on the temporal dimension.

In this paper, we use the term "feature" to indicate the potential variable that fully represents the distribution of interest in any dimension. Additionally, the observational-temporal joint space may also be referred to as "observable data space", in contrast to the "latent feature space".

1.4 Hyper-Dimensional Space

Unobservable relations that fall outside the primary modeling objective can profoundly affect relationship models. This can be traced back to an undetected joint distribution within the hyper-dimensional space.

For example, when evaluating the impact of spicy foods on health, the direct link between spiciness and health is our primary modeling focus. However, there are underlying relations at play - such as how personal traits (individual-level features) are influenced by their cultural context (population-level features). Even if cultural differences are out of our modeling concern, overlooking these hierarchical distributions may introduce biases into our relationship model. For clarity, we term these hidden hyper-dimensional distributions as *unobservable* ***hierarchies***, sidestepping their relational aspects that fall outside the modeling objective.

These unobservable hierarchies often signify different granularity levels within the population. Achieving model ***generalizability*** across these levels is a common concern, dependent on the model's ability to reuse learned lower-level relationships for higher-level learnings Scholkopf et al. (2021). We argue that a shift from *Observation-Oriented* to *Relation-Oriented* is essential to realize this goal, in light of the *relation-centric* nature of human intelligence. In human understanding, relations function as ***indices*** that point to our mental representations Pitt (2022), crafting interconnected knowledge systems in memory, inclusive of their hierarchical structures. In line with this perspective, our proposed *relation-defined representation* learning is conceived as an attempt to "simulate" the process of human knowledge construction.

Chapter I: Deficiency of Current Observation-Oriented Paradigm

This chapter begins by examining the impact of unobservable hierarchies on models in Section 2, to highlight how these hierarchies can result in significant information loss on the temporal dimension, and its challenges for conventional causal inference. In Section 3, we offer a comprehensive critique of the prevailing *Observation-Oriented* causal learning paradigm. Finally, Section 4 delves into the temporal space untouched by the current paradigm, spotlighting its multi-dimensional nature that leads to inherent modeling issues.

2 Impact of Unobservable Hierarchies

Unobservable hierarchies in knowledge suggest unknown distributions in the hyper-dimensional space, which are related to but distinct from the modeling objective. For solely observational learning tasks, such unknowns may lead to troubles, but still have the potential to be uncovered through methods like reinforcement learning. However, when it comes to observational-temporal causal learning, the *Observation-Oriented* paradigm inherently falls short in capturing dynamical temporal features across all hierarchical levels. This section will illustrate these phenomena via two examples: one from computer vision and another from health informatics. For the latter, we will further dissect the issue from a traditional causal inference perspective.

2.1 Observational Hierarchy

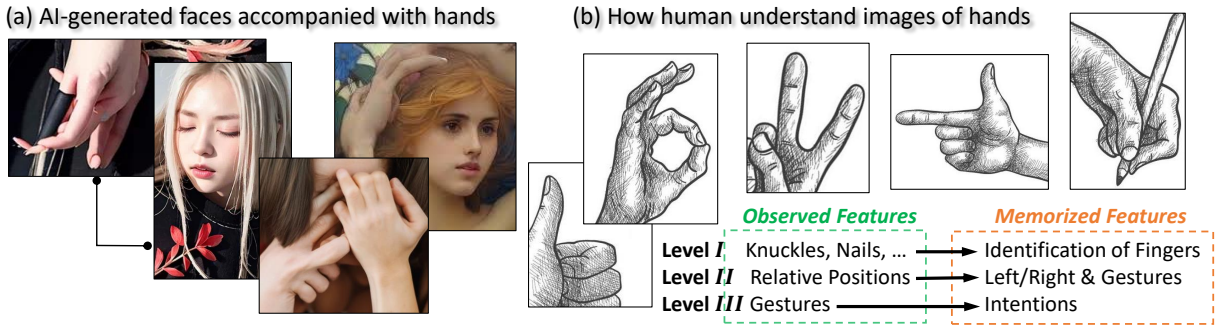

Figure 2: A comparison of AI-generated and human-sketched hand images. AI processes observed features simultaneously, thus treating hands as arbitrary mixtures of finger-like items. The process is hierarchical for humans, indexed through relations, where higher-level recognition relies on lower-level conclusions.

Figure 2(a) showcases AI-created hands with faithful color but unrealistic shapes, while humans can easily recognize a plausible hand from simple grayscale sketches in (b). Indeed, we can rapidly decompose our observations hierarchically according to different relations in our knowledge, and process sequentially from lower to higher levels: **I** identifies fingers through knuckles, nails, and relative lengths; **II** denotes hand gestures through positions; **III** retrieves the gesture's meaning from memory. However, such an intuitive hierarchy exists in our cognitions only. To AI, or similarly, to an extraterrestrial without our knowledge, the hands in Figure 2(a) may seem as reasonable as the actual hands.

Such observational hierarchy may not always create major problems. If features at different levels do not significantly overlap, AI may successfully "distinguish" them. For instance, AI can generate convincing faces because the appearance of eyes is strongly indicative of the facial angle, eliminating the need for AI to recognize "eyes" from "faces". But various hand gestures may have similar appearances, leading to chaos.

Even with problems, AI may learn the hidden knowledge via reinforcement learning Sutton & Barto (2018), under the guidance of human feedback. For example, human approval of five-fingered hands could lead AI to start identifying fingers autonomously. It works because of *completely* captured observational features at each level, while may not function when involving distributions across temporal dimensions.

2.2 Observational-Temporal Hierarchy

Figure 3(a) depicts patients' daily effects on B following $do(A)$, with t indicating the elapsed days. For simplicity, let's assume the patient's (unobserved) personal characteristics linearly influence M_A's release,

i.e., uniformly accelerate or decelerate its effective progress. The individualized causal effects (i.e., the red and blue curves in (a)) are shaped by two levels of *dynamical temporal* features: 1) the population-level effect sequence with a standard length of 30, and 2) the individual-level progress speed. An accurate estimation of the level 1) dynamical feature provides the desired clinical effectiveness evaluation of M_A.

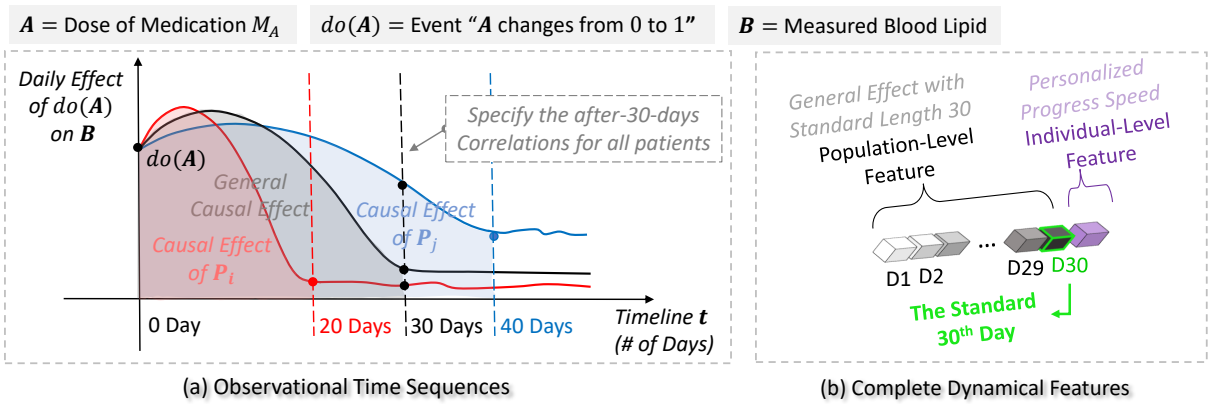

(a) Observational Time Sequences (b) Complete Dynamical Features

Figure 3: Medication M_A treats high blood lipid, with $do(A)$ denoting its initial use. It is given that the population-level effect takes about 30 days to fully manifest ($t = 30$ at the elbow), depicted by the black curve in (a). Patient P_i achieves this effect curve elbow in 20 days, while P_j takes 40 days.

Figure 3(b) represents patients' effects in a 31-length feature vector, disentangled by two hierarchical levels. Traditional medical effect estimation is often obtained by averaging the patients' after-30-day performances. This essentially builds a correlation model $B_{t+30} = f(do(A_t))$, which only captures a *static temporal* feature B_{t+30}, the last step of the level 1) dynamic, disregarding the preceding 29 steps. Moreover, even if the estimation method employs a sequence of length 30 (e.g., Granger causality), it can capture the level 1) dynamic at most and is exclusive of further levels. Causal effects with multiple levels of dynamics are prevalent in various causal learning applications, such as epidemic progression, economic fluctuations, strategic decision-making, etc. The *Observation-Oriented* paradigm necessitates identifying objects before establishing relations, making it often difficult to comprehensively encompass all levels of dynamics.

2.3 Strange Hidden-Confounder in Causal Inference

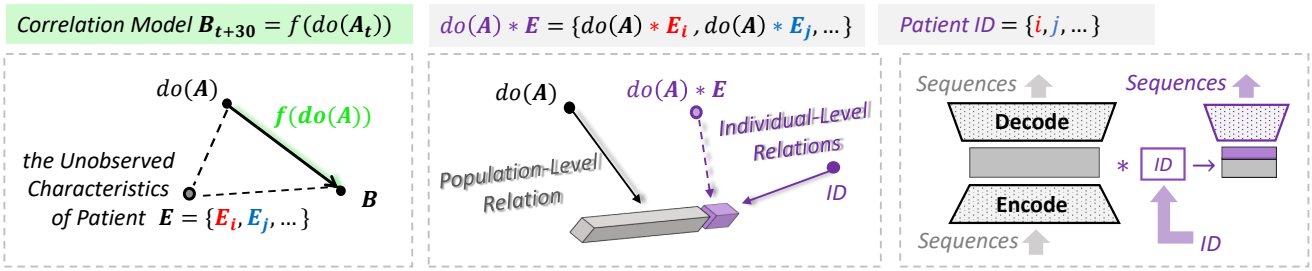

(a) DAG with Hidden Confounder (b) Relation-Oriented Disentanglement (c) Latent Space Representation of (b)

Figure 4: (a) Traditional causal inference DAG. (b) Hierarchical disentanglement of dynamics using relations as indices. (c) Autoencoder-based generalized and individualized reconstructions of the sequential data.

For patients P_i and P_j, the estimated last-day effect B_{t+30} is biased, as P_i exceeds 100% full effect, while P_j only achieves about 75%. To account for such individual-level biases, causal inference usually introduces a *hidden confounder* into DAG (Directed Acyclic Graph), to represent the unobserved personalized characteristics, depicted as the node E in Figure 4 (a), a strangely involved outer variable. It implies an illogical assertion: "Our model is biased due to some unknown aspects we have no intention to know."

It is because, while E is unknown, its effect, the individual-level dynamical feature, is observable, but excluded by the solely observational model f. Although hidden, E is observational and thus could be incorporated by f if revealed. Thus, introducing a hidden confounder transforms *observed dynamical* variables into *unobserved observational* ones, which enhances human understanding but unnecessarily benefits the model.

As depicted in Figure 4(b), traditional causal inference views the individual-level effect as caused by the unobserved composite cause $do(A) * E$, not a directly modelable relationship. Conversely, a *Relation-Oriented* approach just treats relation as an index, to extract representations of *observational-temporal* effects from sequential data, so we can employ any observed identifier, e.g., patient ID. Figure 4(c) illustrates its implementation architecture, to realize a relation-defined hierarchical disentanglement.

3 Causality on Temporal Dimension

Causality research acts as a gateway into the temporal dimension, going beyond the observational space. However, the current causal learning models, formulated as $y_{t+m} = f(x_t)$ for causality $X \to Y$ with m as a predetermined time progression, do not fully integrate t as a computational dimension.

Under the prevailing *Observation-Oriented* paradigm, the objects - cause on X and effect on Y - must be pre-identified prior to formulating the relation function f. While it remains feasible to assign a sequence of X to encompass dynamics for the cause, identifying the exact start and end timestamps for the effect becomes problematic. Consequently, traditional causal inference typically treats effects as solely *observational*, with *static* temporal aspects determined by predefined m. When the underlying effects have *dynamical* significance, selecting an appropriate value for m to capture the most relevant snapshot becomes challenging. This *identifiability difficulty* is further magnified when multiple levels of dynamics are present in effects.

Indeed, integrating the concept of *temporal distribution* could greatly streamline causal inference theories, making associated ideas more intuitive. For instance, when we acquire *Counterfactuals* Pearl (2009), we are essentially capturing temporal distributions in response to conditional queries. Also, as demonstrated in the prior section, fully capturing the observed dynamics across all hierarchical levels within the model could potentially eliminate the need for hidden confounders.

Next, we begin by redefining the notion of causal models concerning the temporal dimension in Section 3.1, then delve into existing methodologies in Section 3.2, focusing on their capacity to capture temporal distributions, with a particular exploration of the essence of do-calculus. Section 3.3 discusses inherent limitations of the dominant *Observation-Oriented* causal model paradigm.

3.1 Redefined Causality Modeling

Traditional causal inference heavily emphasizes interpreting models, such as discerning the causal directions, to distinguish them from mere correlations. In essence, the temporal-evolving aspects that set causality apart from correlation are mainly evident in interpretations, rather than directly within the modeling framework.

From a modeling perspective, once the domain is defined, the learning process does not consider the temporal significance behind the dimensions, including the timestamp attribute. Thus, it is understandable that the traditional paradigm leans heavily on interpretation. With this in mind, we differentiate causality from correlation in the modeling context by integrating distributions along the temporal dimension.

Theorem 1. Causality vs. Correlation in the modeling context.
- Causality is the relationship between *observational-temporal* features, which can be ***dynamical***.
- Correlation is the relationship between features ***not dynamical***.

A causality $X \to Y$ can be divided into two parts: 1) the informative relation connecting X and Y, crucial for modeling, and 2) the causal direction, i.e., the roles of cause and effect, mainly significant in interpretation. Specifically, for model selection, we can employ $Y = f(X; \theta)$ to predict the effect on Y, and, conversely, utilize $X = g(Y; \psi)$ to deduce the cause X given Y. Both parameters, θ and ψ, are derived from the joint probability $\mathbf{P}(X, Y)$ without imposing modeling restrictions.

In practice, the causal direction is often predetermined for models. One reason is the importance of aligning with our intuitive understanding of temporal progression. Moreover, the prevailing causal model paradigm displays an *imbalanced* capacity for capturing dynamical features between the cause X and the effect Y. For example, in Figure 4, inverse modeling of $do(A) = f(\{B_t\})$ through RNNs, given a sufficiently long sequence $\{B_t\} = \{B_{t+1}, \ldots, B_{t+40}\}$, might fully capture dynamics of B and negate the need for a hidden confounder.

Within the suggested *Relation-Oriented* approach, we can utilize relations to accurately identify the effect's observational-temporal features and fully extract their representations. As a result, the modeling function f is relieved from encapsulating temporal facets. The differentiation between causality and correlation becomes a matter of connected features, rather than the nature of the relational model.

3.2 Learning Temporal Distributions

Numerous methods are dedicated to capturing the dynamical features of the ***cause*** alone, such as autoregressive models Hyvärinen et al. (2010) and RNNs Xu et al. (2020), both employing the modeling formate $y_{t+m} = f(\{x_t\})$ with $\{x_t\} = \{x_1, \ldots, x_t, x_{t+1}, \ldots, x_T\}$. Meanwhile, Granger causality Maziarz (2015), a method widely recognized in economics, employs a sequence for the ***effect*** that exhibits significant temporal patterns, in the formate $\{y_\tau\} = f(\{x_t\})$, where t and τ signifying two separate timelines.

Yet, using a sequence does not guarantee capturing dynamics. The distinction between "a sequence of static variables" and "a dynamical variable" hinges on whether the *nonlinear* mutual relationships among these variables can be captured. For autoregressive, if the selected model is linear, then $\{x_t\}$ remains a static sequence. Conversely, RNNs can harness the nonlinearity of $\{x_t\}$, enabling them to encapsulate dynamics even within multiple levels. In Granger causality, the effect sequence $\{y_\tau\}$ must be observationally identified before modeling, making it typically a static sequence. At best, it can capture a single-level dynamic with the right parameter setting, e.g., referring to Figure 3(b), a *30-length* average sequence may capture level 1).

A more universal approach to represent temporal distributions is do-calculus Pearl (2012); Huang & Valtorta (2012). Instead of specifying time sequences, it takes the *identifiable* temporal events as modeling objects to conduct elementary calculus. The $do(\cdot)$ format flexibly modulates temporal features for the ***cause***. However, such a *differential*-calculus essence also introduces elevated complexity. Here, we reinterpret its three core rules from an *integral*-calculus perspective, aiming for a more intuitive comprehension.

For the time sequence $\{x_t\} = \{x_1, \ldots, x_T\}$, let $do(x_t) = \{x_t, x_{t+1}\}$ indicate the occurrence of an instantaneous event $do(x)$ at time t. Time lag Δt between $\{t, t+1\}$ is sufficiently small to make this event identifiable, such that $do(x_t)$'s *interventional* effect can be depicted as a function of the resultant distribution at $t+1$. Conversely, the effect provoked by static x_t snapshot is called *observational* effect. Then, the observational-temporal distribution of the cause $X \in \mathbb{R}^d$ can be formulated as below:

Given $\mathcal{X} \to Y \mid Z$, where $\mathcal{X} = \langle X, t \rangle \in \mathbb{R}^{d+1}$ encompass the temporal dimension, we have

$$\mathcal{X} = \int_0^T do(x_t) \cdot x_t \; dt \quad \text{with} \begin{cases} (do(x_t) = 1) \mid do(z_t), & \textit{Observational} \text{ only (Rule 1)} \\ (x_t = 1) \mid do(z_t), & \textit{Interventional} \text{ only (Rule 2)} \\ (do(x_t) = 0) \mid do(z_t), & \text{No } \textit{interventional} \text{ (Rule 3)} \\ \text{otherwise} & \text{Associated } \textit{observational} \text{ and } \textit{interventional} \end{cases}$$

The effect of $\mathcal{X}$ can be derived as $f(\mathcal{X}) = \displaystyle\int_0^T f_t\big(do(x_t) \cdot x_t\big) \; dt = \sum_{t=0}^{T-1} (y_{t+1} - y_t) = y_T - y_0$

Within the graphical system $\{X, Y, Z\}$, the rules of do-calculus tackle three specific scenarios (notably, a specifiable $do(x_t) \cdot x_t$ pertains to Rule 2), where conditional independence is maintained between the *observational* and *interventional* effects. However, these rules bypass more generalized cases.

Utilizing the $do(\cdot)$ format, we can also represent observational-temporal distributions of Y as $\mathcal{Y} = \langle Y, \tau \rangle$, by incorporating an additional timeline τ. However, in the *Observation-Oriented* paradigm, identifiable events for $\mathcal{Y}$ still necessitate our prior specifications. In contrast, the proposed *Relation-Oriented* approach can autonomously construct $\mathcal{Y}$ via relation-indexing.

3.3 Limitation of Current Causal Model Paradigm

Our innate understanding of causality aligns with Theorem 1. Yet, confining causal models to the observational space can lead to potential misalignments between these models and our intuitive knowledge. We have categorized causal modeling into four scenarios shown in Figure 5. Depending on whether the relationship

is already in knowledge, the modeling queries can be divided into causal discovery, which seeks new insights, and causal learning, which leverages knowledge to model causality. Further, these applications can be categorized based on the dynamical significance of the effects. For instance, the causality "raining → wet floor" includes only static temporal features, which is logically a causality but not distinguishable from correlation once modeled. We explore these scenarios from two perspectives: the *relation* connecting features, critical for modeling, and the *causal direction*, essential for interpretation.

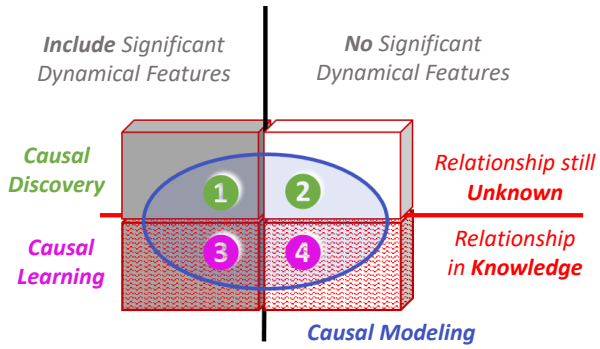

	Modeled Relation	Modeled Causal Direction
1	Observational Only. Undiscovered Dynamics covered by *Faithfulness Assumption.*	Observational Information Determined. Not Logical Causal Meaningful.
2	Observational Only. Aligned with Knowledge.	Observational Information Determined. Maybe Logical Causal Meaningful.
3	Knowledge Determined. Unmodeled Dynamics covered by *Hidden Confounders* or *Sufficiency Assumption.*	Knowledge Determined.
4	Knowledge Determined.	Knowledge Determined.

Figure 5: An overview of the current *Observation-Oriented* causal model paradigm. On the left, the rectangle means all logical causal relationships, while its potentially modelable scope is blue-circled.

(1) Modeled Relation

Traditional causal inference has made notable advancements in "downgrading" dynamical temporal features to be observationally accessible. For instance, do-calculus explores independence conditions on the temporal dimension. For overlooked dynamical features of the effect, if existing knowledge can suggest its potential cause, creating a hidden confounder can enhance comprehension; if not, these dynamics may be dismissed based on the *causal Sufficiency assumption*, potentially leading to subsequent challenges.

On the other hand, causal discovery mainly scans the observational space to explore dependencies. As a result, if the underlying causality does not encompass significant dynamics, causal discovery can be effective. However, if such dynamics exist, they largely go undetected. This potential gap may be negated under the *causal Faithfulness assumption* suggesting that observed variables fully represent the causal reality.

(2) Modeled Causal Direction

Consider observed variables X and Y in a graphical system, with specified models $Y = f(X;\theta)$ and $X = g(Y;\psi)$. Based on observations, the discovered causal direction between X and Y is determined by the likelihoods of estimated parameters $\hat{\theta}$ and $\hat{\psi}$. Given the joint distribution $\mathbf{P}(X,Y)$, one would prefer $X \to Y$ if $\mathcal{L}(\hat{\theta}) > \mathcal{L}(\hat{\psi})$. Now, let $\mathcal{I}(\theta)$ be a simplified form of $\mathcal{I}_{X,Y}(\theta)$, the Fisher information, representing the amount of information contained by $\mathbf{P}(X,Y)$ about unknown θ. Assume $p(\cdot)$ to be the probability density function; then, in this context, $\int_X p(x;\theta)dx$ remains constant. So, we have

$$\mathcal{I}(\theta) = \mathbb{E}[(\frac{\partial}{\partial\theta}\log p(X,Y;\theta))^2 \mid \theta] = \int_Y\int_X (\frac{\partial}{\partial\theta}\log p(x,y;\theta))^2 p(x,y;\theta)dxdy$$

$$= \alpha\int_Y (\frac{\partial}{\partial\theta}\log p(y;x,\theta))^2 p(y;x,\theta)dy + \beta = \alpha\mathcal{I}_{Y|X}(\theta) + \beta, \text{with } \alpha,\beta \text{ constants.}$$

$$\text{Thus, } \hat{\theta} = \arg\max_\theta \mathbf{P}(Y \mid X,\theta) = \arg\min_\theta \mathcal{I}_{Y|X}(\theta) = \arg\min_\theta \mathcal{I}(\theta), \text{ and } \mathcal{L}(\hat{\theta}) \propto 1/\mathcal{I}(\hat{\theta}).$$

Subsequently, the likelihoods of the estimated parameters $\hat{\theta}$ and $\hat{\psi}$ depend on the amount of information, $\mathcal{I}(\hat{\theta})$ and $\mathcal{I}(\hat{\psi})$. That means the learned directionality between X and Y essentially indicates how much their specified distributions are reflected in the data, with the more dominant one deemed the "cause". It presumes that the cause is more comprehensively captured in the observations than the effect by default. Due to restricted data collection techniques, such a presumption was justifiable in past decades. But in the present era, assuming such discovered directions to have logical causal meaning is no longer appropriate.

4 The Overlooked Temporal Space

Data is commonly stored in matrices, with time series data incorporating an extra attribute for the timestamps, which forms a logical timeline to reflect the absolute time evolution in reality. Traditionally, modeling has relied on this timeline to determine the chronological order of all potential events. However, our intuitive understanding of time is far more complex than this singular, simplified absolute timeline.

Consider an analogy where ants dwell on a two-dimensional plane of a floor. If these ants were to construct models, they might use the nearest tree as a reference to specify the elevation in their two-dimensional models. By modeling, they observe an increased disruption at the tree's mid-level, which indicates a higher chance of encountering children. However, since they fail to comprehend humans as three-dimensional beings, instead of interpreting this phenomenon in a new dimension "height", they solely relate it to the tree's mid-level. If they migrate to a different tree with a varying height, where mid-level no longer presents a risk, they might conclude that human behavior is too complex to model effectively. Similarly, when modeling time series, we usually discount the dimension "time" as the single absolute timeline, which has become our "tree".

Our understanding allows for the simultaneous existence of multiple logical timelines. If one is designated as the absolute timeline, the remaining ones can be viewed as relative timelines, each representing distinctive temporal events, which can be interconnected via specific relationships. In such *Relation-Oriented* perspective, like, during a causal inference analysis, the temporal dimension contains numerous possible logical timelines that we could choose to construct any necessary scenarios. However, once we enter a modeling context, like, using AI to model the time series along a single timeline, the temporal significance no longer exists, but only a regular dimension containing timestamp values, indistinguishable from other observational attributes. Metaphorically, if we consider the observational space for AI modeling as Schrödinger's box and our interest is the "cat" within, our task is to accurately construct the box, giving adequate consideration to all potential logical timelines, to ensure the "cat" remains *reasonable* upon unveiling.

Theorem 2. The term *Temporal Dimension* encompasses all potential logical timelines, not just a singular one. Consequently, a *Temporal Space* is defined as the space built by chosen timeline axes.

Fundamentally, as three-dimensional beings, we are limited from truly understanding temporal dimensionality. As the term "space" typically evokes a three-dimensional conception, the notion of "temporal space" might seem odd for a four-dimensional creature. Like ants can use trees as references without the need to fully comprehend the third dimension, we rely on logical timelines to interpret the fourth. At this juncture, our mission is to recognize the potential "forest" beyond the present single "tree".

This section will demonstrate how the single-timeline-based timestamp specification operation, rooted in the *Observation-Oriented* paradigm, inherently biases modeling and hinders model generalizability. Then we will summarize advancements and challenges on our journey towards realizing causal knowledge-aligned AI.

4.1 Inherent Temporal Bias Scheme

Modeling event identification typically relies on timestamps derived from a singular timeline in time series data. In structural causal models (SCMs), this can induce *inherent temporal biases*, limiting our capacity to leverage AI's potential in the temporal dimension. This issue becomes more acute in large-scale causal relationships, where more logical timelines may be hidden.

To better ascribe this issue, we improve the causal DAG (directed acyclic graph) Pearl (2009) as follows: **1)** incorporating (potentially multiple) logical timelines as axes into the DAG space, and **2)** defining edges along timeline axes to be vectors with meaningful lengths indicating the timespans of causal effects. For example, the single-timeline scenario in Figure 3 has the new DAG depicted in Figure 6(b), with (a) showing the traditional one as a comparison. The edge $do(A) \rightarrow B$ in Figure 6(a) represents the population-level effect only, thus necessities a hidden confounder to explain the individual-level diversities, while in Figure 6(b), they can be explicitly represented by varying lengths of $\overrightarrow{do(A)\ B}$.

Consider an expanded two-timeline scenario in Figure 7(a), where A shorthandly represents $do(A)$. Apart from its primary effect on B, A also indirectly influences B through its side effect on another vital sign, C,

depicted as edges $\overrightarrow{AC}$ and $\overrightarrow{CB}$. For simplicity, assume the timespan for $\overrightarrow{AC}$ is 10 days for all patients, with the individual-level diversity confined to timeline T_X alone. In conventional single-timeline causal modeling, the SCM function would be $B_{t+30} = f(A_t, C_{t+10})$. Let's assume $f(A_t, C_{t+10})$ is implemented using RNNs, which can accurately depict the individual-level final effects of A on B for any patient.

The confounding relationship over nodes $\{A, B, C\}$ forms a triangle across timelines T_X and T_Y - such shape geometrically holds for any hierarchical level relationship. For patients P_i and P_j, the *individualization* process is to "stretch" this triangle along T_X by different ratios, which is a homographic *linear transformation* in this space. However, as illustrated in Figure 7 (b) and (c), for either P_i or P_j, equating the outcome of f to be B_{t+30} violates the *causal Markov condition* necessary for reasonable SCMs.

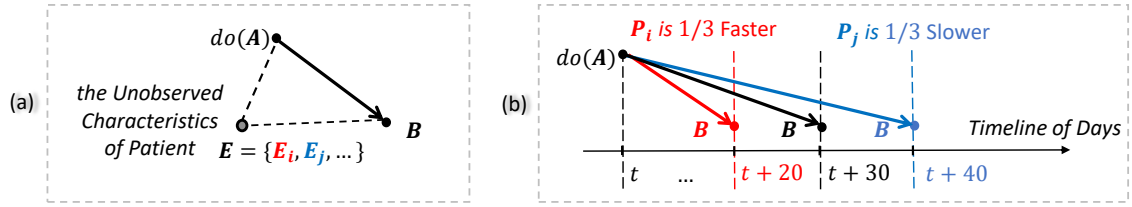

Figure 6: (a) Traditional Causal DAG introducing hidden E. (b) Improved DAG: the standard black vector signifies the population-level effect, while the individual-level ones are represented by its different scaling.

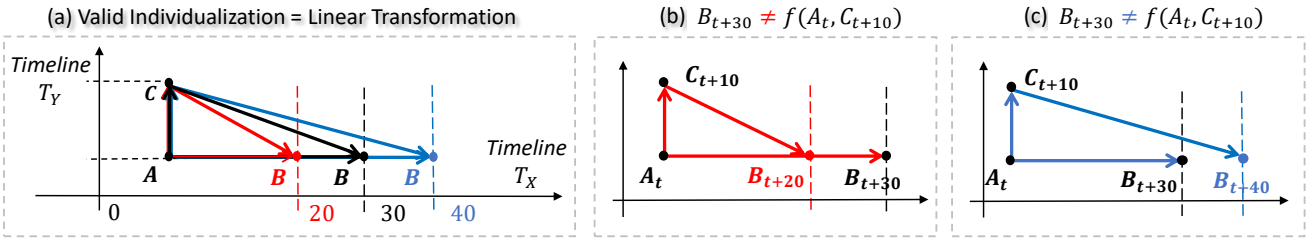

Figure 7: (a) A two-timeline DAG space, where a valid individualization presents a linear transformation. (b)(c) Violations of the Markov condition for the prevailing SCM with confounding dynamics across timelines.

Notably, in this specific case, the violation may not cause significant issues for AI models like RNNs. Given the *independence* of dynamics on T_X and T_Y, the SCM can be formulated as $B_{t+30} = f_1(A_t) + f_2(C_{t+10})$, suggesting that the cross-timeline confounding can be broken down into two single-timeline issues. However, making assumptions such as independence or non-confounding is unrealistic. Since each cause-and-effect pair might possess its unique logical timeline, these inherent temporal biases can accumulate exponentially, significantly impacting the robustness of causal models, irrespective of our model selections.

Theorem 3. The ***inherent*** *temporal bias* may occur in SCM if it contains: **1)** *Confounding* dynamical temporal features across *Multiple* logical timelines, and **2)** Unobservable hierarchy.

It is interesting to notice that most of the successful causal applications instinctively avoid one of the two factors: *confounding* or *multi-timeline*. Statistical causal models can facilitate de-confounding as a pre-processing, e.g., the backdoor adjustment Pearl (2009). For AI models, most of the achievements do not potentially involve relative timelines, e.g., the large language model (LLM) in a semantic space, where the phrases are ordered consistently along a single logical timeline.

Unlike AI's black-box nature, causal inference essentially takes a *Relation-Oriented* viewpoint. Nevertheless, in its context, the inherent temporal biases are difficult to recognize, as they often intermingle with the modeling biases resulting from the statistically unsolvable nonlinearity. They have similar manifestations, and both can be addressed by de-confounding. Consider Figure 6(a), the linearly modeled population-level effect mismatches with individuals P_i and P_j, which may not be distinguishable from the mismatching that occurs in Figure 7(b)(c), caused by dynamics across multi-timelines.

4.2 Inherent Impact on SCM Generalizability

Traditional SCMs usually require specifying timestamps for objective events before modeling relations. While this affects model robustness, the more pressing concern is that neglecting multiple timelines can render established SCMs non-generalizable across different scenarios with analogous core relationships.

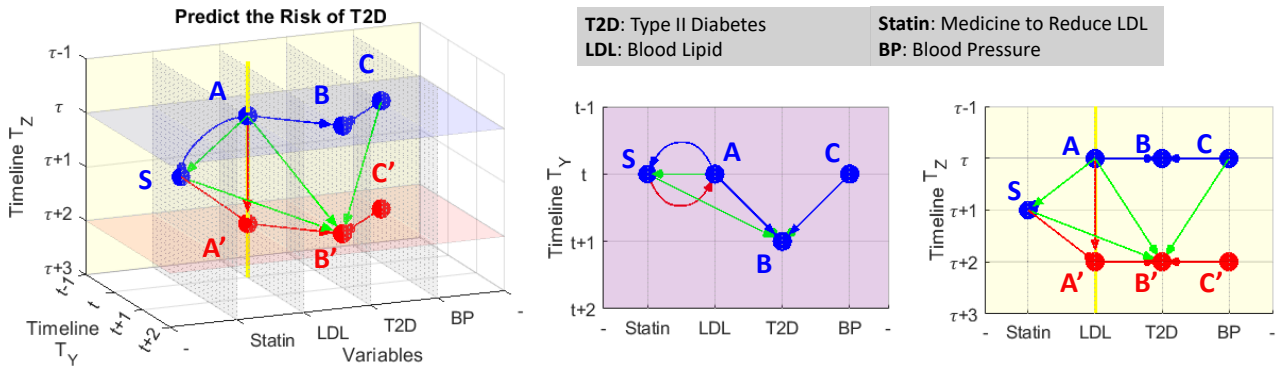

Figure 8: An exemplified 3D observational-temporal DAG space, with specified SCM, $B' = f(A, C, S)$, to evaluate Statin's medical effect on reducing the risk of T2D, including two logical timelines $\mathcal{T}_Y$ and $\mathcal{T}_Z$. On $\mathcal{T}_Y$, the step Δt from t to $(t+1)$ allows A and C to fully influence B, while the step $\Delta\tau$ on $\mathcal{T}_Z$, from $(\tau+1)$ to $(\tau+2)$, let medicine S completely release its effect to progress from A to A'.

Consider the practical scenario depicted in Figure 8. Here, Δt and $\Delta\tau$ represent actual time spans. Yet, the crux is not on determining their exact values, but on realizing their intended causal relationship: As each unit of Statin's effect is delivered on LDL via $\overrightarrow{SA'}$, it immediately impacts T2D through $\overrightarrow{A'B'}$. Simultaneously, the next unit effect begins generation. This dual action runs concurrently until S is fully administered. At B', the ultimate aim of this process is to evaluate the total cumulative influence stemming from S.

Given the relationship $\overrightarrow{SB'} = \overrightarrow{SA'} + \overrightarrow{A'B'}$, specifying the $\overrightarrow{SB'}$ time span (i.e., half of the $\overrightarrow{AB'}$ time span) inherently sets the $\Delta t : \Delta\tau$ ratio, defining the ASB' triangle's shape in this DAG space. While the estimated mean effect at B' might be precise for the present population, the preset $\Delta t : \Delta\tau$ ratio's universality is questionable, potentially constraining the established SCM's generalizability.

4.3 Toward Causal Knowledge-Aligned AI

Our quest for causal reasoning AI involves broadening our modeling techniques from solely observational to include temporal dimensions, as summarized in Figure 9. The present challenge lies in enabling structural causal models in the joint observational-temporal feature space. Recognizing underlying logical timelines is critical to avoid inherent biases and enhance model generalizability. However, since manual identification is unrealistic, it may have been time for us to consider the new paradigm.

The initial models under i.i.d. assumption only approximate observational associations, proved unreliable for causal reasoning Pearl et al. (2000); Peters et al. (2017). Correspondingly, the common cause principle highlights the significance of the nontrivial conditional properties, to distinguish structural relationships from statistical dependencies Dawid (1979); Geiger & Pearl (1993), providing a basis for effectively uncovering the underlying structures in graphical models Peters et al. (2014).

Graphical causal models relying on conditional dependencies to construct Bayesian networks (BNs) often operate in observational space and neglect temporal aspects, reducing their causal relevance Scheines (1997). Causally significant models, such as Structural Equation Models (SEMs) and Functional Causal Models (FCMs) Glymour et al. (2019); Elwert (2013), can address counterfactual queries Scholkopf et al. (2021), with respect to temporal distributions by leveraging prior knowledge, to construct causal DAGs accordingly.

State-of-the-art deep learning applications on causality, which encode the DAG structural constraint into continuous optimization functions Zheng et al. (2018; 2020); Lachapelle et al. (2019), undoubtedly enable

highly efficient solutions, especially for large-scale problems. However, larger question scales indicate more underlying logical timelines, which may lead to snowballing temporal biases. It can be evident from the limited successful applications of incorporating DAG structure into network architectures Luo et al. (2020); Ma (2018), e.g., neural architecture search (NAS).

Model	*Principle*	*Cause*	*Connection & Direction*	*Effect*	*Handle Unobservable Hierarchy*	*Capture Dynamics*
Mechanistic or Physical	$\mathcal{Y} = f(\mathcal{X};\theta)$	Observational-Temporal $\mathcal{X} = \langle X, t\rangle$	by Knowledge	Observational-Temporal $\mathcal{Y} = \langle Y, t\rangle$	Yes	Yes
Relation-Oriented Structural Model	*Given* $\boldsymbol{P}(\mathcal{X},\mathcal{Y})$ & $\mathcal{X} \to \mathcal{Y}$	Observational-Temporal $\mathcal{X} = \langle X, t\rangle$	Learn Representation $\hat{\mathcal{Y}} = f(\mathcal{X};\theta)$	Observational-Temporal $\hat{\mathcal{Y}} = \langle \hat{Y}, t\rangle$	Yes	Yes
Structural Causal Learning	*Given* $\boldsymbol{P}(X,Y)$ & $X \to Y$ $Y = f(X;\theta)$	Observational Sequence $\{X_t\}$	Connected via θ $X \to Y$ by Knowledge	Observational and Static Y_t	?	?
Graphical Causal Discovery	*Given* $\boldsymbol{P}(X,Y)$ *Find* $\mathcal{L}(Y\|X;\theta) > \mathcal{L}(X\|Y;\theta)$	Observational X	Connected via θ $X \to Y$ by Observed Info	Observational Y	?	No
Common Cause Model	*Given* $\boldsymbol{P}(X,Y\|Z)$	Observational X	Connected via Z	Observational Y	?	No
i.i.d Data Driven Model	*Given* $\boldsymbol{P}(X,Y)$	Observational X	None	Observational Y	No	No

Figure 9: Simple Taxonomy of Models (Adapted in part of Table 1 in Scholkopf et al. (2021)), from more knowledge-driven (top in purple) to more data-driven (bottom in green). Notations: θ = parameter derived from joint or conditional distribution, $\langle X, t\rangle$ = augment t-dimension, "?" = depending on practice.

Schölkopf Scholkopf et al. (2021) summarized three key challenges impeding causal AI applications to achieving generalizable success: 1) limited model robustness, 2) insufficient model reusability, and 3) inability to handle data heterogeneity (caused by unobservable hierarchies in knowledge). Notably, all these challenges can be attributed to the timestamp specification required by *Observation-Oriented* structural models.

On the other side, physical models, which explicitly integrate temporal dimensions in computation, and are able to establish abstract concepts through relations, may provide insights into these challenges. We believe that the *Relation-Oriented* approach can help bridge the gap between observational and temporal spaces.

Chapter II: Realization of Proposed Relation-Oriented Paradigm

This chapter begins by formulating the factorizations to achieve hierarchical disentanglement in the latent space. Then, we explore the proposed *relation-defined representation* methodology as an embodiment of the *Relation-Oriented* paradigm. Lastly, we validate its efficacy through comprehensive experiments.

5 Hierarchical Disentanglement in Latent Space

Given an observational variable $X \in \mathbb{R}^d$, we denote its time sequence of length T as $\{x_t\} = \{x_1, \ldots, x_{t-1}, x_t, x_{t+1}, \ldots, x_T\}$. Our goal is to construct a latent feature space $\mathbb{R}^L$ for two specific purposes: 1) Fully represent the observational-temporal features of $\mathcal{X} = \langle X, t\rangle \in \mathbb{R}^{d+1}$. 2) Hierarchically disentangle $\mathcal{X}$'s representation according to relations in knowledge. Consequently, the established system realizes the reusability of models at any hierarchical level by indexing through the corresponding relations.

For $\mathcal{Y} = \langle Y, \tau\rangle \in \mathbb{R}^{b+1}$, if the relationship $\mathcal{X} \to \mathcal{Y}$ identifies certain features of $\mathcal{Y}$'s distribution, the proposed *relation-defined representation* learning aims to extract the representation $\hat{\mathcal{Y}}$ as determined by the relation with $\mathcal{X}$. Moreover, the resulting $\hat{\mathcal{Y}}$ should be reusable in developing subsequent levels of $\mathcal{Y}$'s representations, thereby facilitating the generalizability of the relationship model for $\mathcal{X} \to \mathcal{Y}$. For instance, in a graphical system $\{\mathcal{X}, \mathcal{Y}, \mathcal{Z}\}$ with relationship $\mathcal{X} \to \mathcal{Y} \leftarrow \mathcal{Z}$, $\mathcal{Y}$ can be viewed as in a two-level hierarchy. The first level is defined by $\mathcal{X} \to \mathcal{Y}$ and the second by $\langle \mathcal{X}, \mathcal{Z}\rangle \to \mathcal{Y}$, where the second level enhances the first by incorporating an additional data stream from $\mathcal{Z}$.

5.1 Factorize Observational-Temporal Hierarchy

Let $X = (X_1, \ldots, X_d) \in \mathbb{R}^d$, and assume $\mathcal{X} = \langle X, t \rangle \in \mathbb{R}^{d+1}$ has an n-level hierarchy. Define Θ_i as the i-th level component of $\mathcal{X}$ in the *observable data space*, and its counterpart in the *latent feature space* $\mathbb{R}^L$ as θ_i. The representation function f_i facilitates the transformation from $\mathbb{R}^{d+1}$ to $\mathbb{R}^{L_i}$ for the i-th level, considering all prior lower-level features as attributes. θ_i is a vector in $\mathbb{R}^L$, with its significant value residing in a subset of the L dimensions, denoted as $\mathbb{R}^{L_i}$, forming the disentanglement $\{\mathbb{R}^{L_1}, \ldots, \mathbb{R}^{L_i}, \ldots, \mathbb{R}^{L_n}\}$. Then, we obtain:

$$\mathcal{X} = \sum_{i=1}^{n} \Theta_i, \text{ where } \Theta_i = f_i\big(\theta_i;\ \Theta_1, \ldots, \Theta_{i-1}\big) \text{ with } \Theta_i \in \mathbb{R}^{d+1} \text{ and } \theta_i \in \mathbb{R}^{L_i} \subseteq \mathbb{R}^L \tag{1}$$

To illustrate an observational hierarchy, refer to Figure 2 (b). Let $\theta_1 \in \mathbb{R}^{L_1}$, $\theta_2 \in \mathbb{R}^{L_2}$, and $\theta_3 \in \mathbb{R}^{L_3}$ represent the three levels of features, with each subspace being mutually exclusive. That is, $L = L_1 + L_2 + L_3$. The combined vector $\langle \theta_1, \theta_2, \theta_3 \rangle \in \mathbb{R}^L$ represent the whole image. In correspondence, Θ_1, Θ_2, and Θ_3 are full-scale images, each presenting unique content. For instance, Θ_1 highlights the details of the fingers, whereas $\Theta_1 + \Theta_2$ expands to showcase the entire hand.

In the context of an observational-temporal hierarchy, the component $\Theta_i \in \mathbb{R}^{d+1}$ can be expressed as the original time sequence $\{\Theta_t\}_i = \{\Theta_{t_i} \in \mathbb{R}^d \mid t_i = 1, \ldots, T\}$. Consequently, we obtain a set of relative logical timelines $\{t_1, \ldots, t_i, \ldots, t_n\}$ which, in contrast to the absolute timeline t, are each uniquely determined by the relationship at their respective levels. However, in the *observable data space*, the i-th level observational-temporal feature, represented as the sum $\Theta_1 + \ldots + \Theta_i$, still maintains its timestamp attribute along t.

5.2 Factorize Hierarchy of Relationship

Given a set of n-level hierarchical representation functions for $\mathcal{X}$, denoted by $\mathcal{F}(\vartheta) = \big\{f_i\big(\theta_i\big) \mid i = 1, \ldots, n\big\}$, our goal is to define n relationship functions, collectively termed $\mathcal{G}$, such that $\mathcal{Y} = \mathcal{G}(\mathcal{X})$ exhibits an n-level hierarchy. Each i-th level relationship function is $g_i(\mathcal{X}; \varphi_i)$, where φ_i is its parameter. Then, we have:

$$\mathcal{G}(\mathcal{X}) = \sum_{i=1}^{n} g_i(\mathcal{X}; \varphi_i) = \sum_{i=1}^{n} g_i(\Theta_i; \varphi_i) = \sum_{i=1}^{n} g_i\big(\theta_i;\ \Theta_1, \ldots, \Theta_{i-1}, \varphi_i\big) = \mathcal{Y} \tag{2}$$

The i-th level relation-defined representation for $\mathcal{Y}$ is $g_i(\theta_i; \varphi_i)$ considering the features of the preceding $(i-1)$ levels of $\mathcal{X}$. This relationship can be portrayed as the augmented feature vector $\langle \theta_i, \varphi_i \rangle$ in latent space $\mathbb{R}^L$. Using ϑ_X and ϑ_Y to distinguish the collective hierarchical representations for $\mathcal{X}$ and $\mathcal{Y}$ respectively, the overall relationship from $\mathcal{X}$ to $\mathcal{Y}$ becomes $\vartheta_Y = \langle \vartheta_X, \varphi \rangle$, where $\varphi = \{\varphi_1, \ldots, \varphi_n\}$. The term $\langle \vartheta_X, \varphi \rangle$ represents the pairwise augmentations between collections ϑ_X and φ.

6 Relation-Defined Representation Methodology

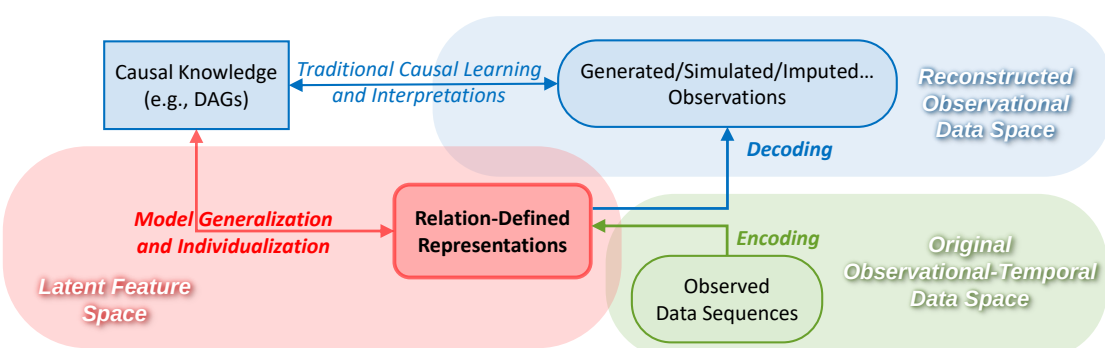

Figure 10: Framework of utilizing *relation-defined representations* to benefit conventional models.

While the existing *Observation-Oriented* modeling paradigm has its limitations, it still forms the basis of many existing knowledge infrastructures. As showcased in Figure 10, relation-defined representations

enable AI to create generalizable models in a latent space rich with human-indecipherable features, and concurrently, AI's potential can be utilized to refine observations, thereby fortifying traditional models through counterfactual effects, de-confounded simulations, and more.

This section presents a specialized autoencoder architecture essential for implementing relation-defined representation; then, outlines the methodology for disentangling hierarchical levels of representations in constructing graphical models. Finally, we introduce a causal discovery algorithm for the latent feature space.

6.1 Invertible Autoencoder for Higher-Dimensional Representation

Autoencoders are generally used for dimensionality reduction, often aligning all observational variables as data attributes for this purpose in structural modeling Wang et al. (2016). However, our objective diverges. We aim to model individual relationships to disentangle variables' representations and simultaneously "stack" them to form a DAG within the latent space, $\mathbb{R}^L$. This space must be large enough to accommodate potential relationships in the form of $\vartheta_Y = \langle \vartheta_X, \varphi \rangle$. This poses a substantial technical challenge, as we need to achieve higher-dimensional representation extraction for individual variables.

Corollary 1. For a given graph G and a data matrix $\mathbf{X}$, which is column-augmented by all observational attributes and timestamps of variables in G, the dimensionality L of the latent space must be at least as large as $rank(\mathbf{X})$ to adequately represent G.

Corollary 1 stems from the notion that the autoencoder-learned $\mathbb{R}^L$ is spanned by $\mathbf{X}$'s top principal components, often referred to in Principal Component Analysis (PCA) Baldi & Hornik (1989); Plaut (2018); Wang et al. (2016). Hypothetically, reducing L below $rank(\mathbf{X})$ may yield a less adequate but causally more significant latent space through better alignment Jain et al. (2021) (further exploration is needed). In this study, we will set aside discussions on the boundaries of dimensionality. Our experiments feature 10 variables with dimensions 1 to 5 (Table 1), and we empirically fine-tune and reduce L from 64 to 16.

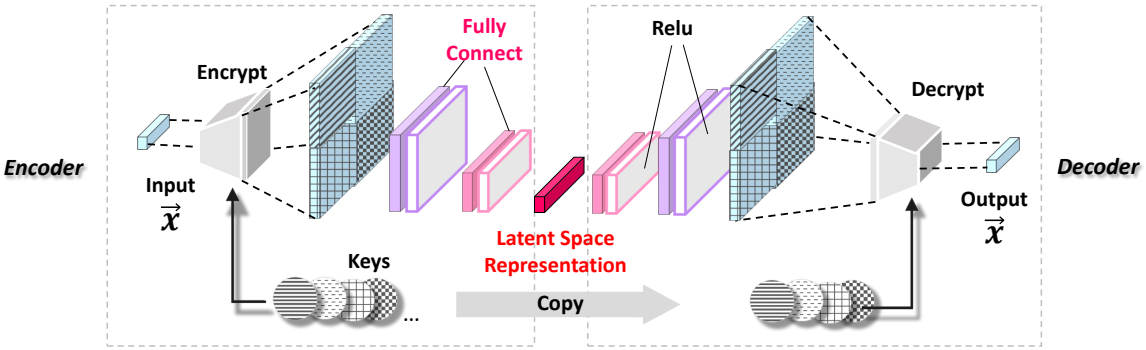

Figure 11: *Invertible* autoencoder architecture for extracting *higher-dimensional* representations.

Figure 11 depicts the proposed autoencoder architecture, featured by the symmetrical *Encrypt* and *Decrypt* layers. Encrypt amplifies the input vector $\vec{x}$ by extracting its higher-order associative features; conversely, Decrypt symmetrically reduces dimensionality and restores $\vec{x}$ to its original form. To ensure reconstruction accuracy, the ***invertibility*** of these operations is naturally required.

Figure 11 illustrates a *double-wise* associative feature expansion, where each pair of *two* digits from $\vec{x}$ are encoded to form a new digit, by associating with a randomized constant *Key*, which is created by the encoder and mirrored by the decoder. A double-wise expansion on $\vec{x} \in \mathbb{R}^d$ generates a $(d-1)(d-1)$ length vector. By using multiple *Keys* and augmenting the derived vectors, $\vec{x}$ can have a significantly extended dimensionality.

The four differently patterned blue squares represent the vectors expanded by four distinct *Keys*, with the grid patterns indicating their "signatures". Each square visualizes a $(d-1)(d-1)$ length vector (not signifying a 2-dimensional vector). In a similar way, higher-order extensions, such as *triple-wise* ones across every three digits, can also be employed by appropriately adapting *Keys*.

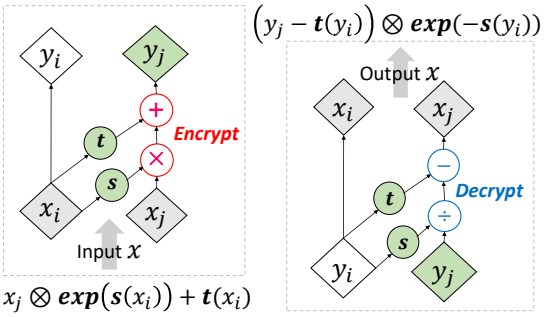

Figure 12: Encrypt (left) and Decrypt (right).

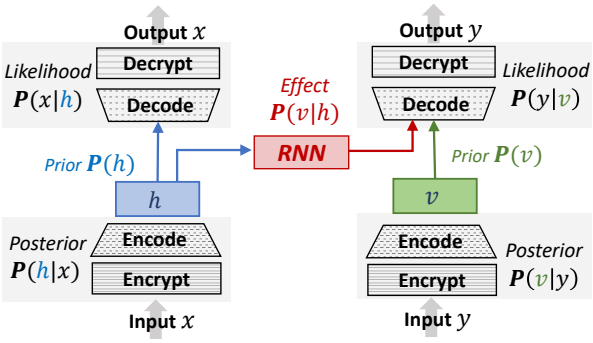

Figure 13: Relationship model architecture.

Figure 12 depicts the encryption and decryption processes used to expand a digit pair (x_i, x_j), where $i \neq j \in 1, \ldots, d$. The encryption function $f_\theta(x_i, x_j) = x_j \otimes exp(s(x_i)) + t(x_i)$ is defined by two specific elementary functions, $s(\cdot)$ and $t(\cdot)$. The parameter θ, serving as a *Key*, consists of their respective weights, $\theta = (w_s, w_t)$.

Specifically, the encryption of (x_i, x_j) transforms x_j into a new digit y_j using x_i as a selected attribute. The decryption process symmetrically employs the inverse function f_θ^{-1}, defined as $(y_j - t(y_i)) \otimes exp(-s(y_i))$. Notably, this approach sidesteps the need to calculate s^{-1} or t^{-1}, allowing $s(\cdot)$ and $t(\cdot)$ to be flexibly specified as needed for nonlinear transformations. This design is inspired by the pioneering work of Dinh et al. (2016) on invertible neural network layers that utilize bijective functions.

By collectively representing all f_θ functions as $\mathcal{F}(X; \vartheta)$, where ϑ encompasses all parameters, the Encrypt and Decrypt layers can be denoted as $Y = \mathcal{F}(X; \vartheta)$ and $X = \mathcal{F}^{-1}(Y; \vartheta)$, respectively. The source code for both Encrypt and Decrypt is provided [1], along with a comprehensive experimental demo.

6.2 Stacking Hierarchical Representations to form SCM

Consider a causal system comprising three variables $\{\mathcal{X}, \mathcal{Y}, \mathcal{Z}\}$, each with corresponding representations $\{\mathcal{H}, \mathcal{V}, \mathcal{K}\} \in \mathbb{R}^L$ initially extracted by three separate autoencoders. Figure 13 illustrates the process of linking $\mathcal{H}$ and $\mathcal{V}$ to model the relationship $\mathcal{X} \to \mathcal{Y}$. Additionally, Figure 14 depicts how two modeled relationships related to $\mathcal{Y}$ are stacked to form a hierarchically disentangled representation.

Consider instances x and y for the relationship $\mathcal{X} \to \mathcal{Y}$, which are represented as h and v in $\mathbb{R}^L$. To estimate the latent dependency $\mathbf{P}(v|h)$, we use an RNN, as shown in Figure 13, to explicitly include the temporal features of h. For the time being, we allow $\mathcal{V}$ to autonomously capture any potential dynamics, with the expectation of future refinements. Each iteration of the learning process involves three optimizations:

1. Optimizing encoder $\mathbf{P}(h|x)$, RNN model $\mathbf{P}(v|h)$, and decoder $\mathbf{P}(y|v)$ to reconstruct $x \to y$ relation.
2. Fine-tuning encoder $\mathbf{P}(v|y)$ and decoder $\mathbf{P}(y|v)$ to accurately represent y.
3. Fine-tuning encoder $\mathbf{P}(h|x)$ and decoder $\mathbf{P}(x|h)$ to accurately represent x.

Throughout the learning, h and v values are iteratively refined to minimize their distance in $\mathbb{R}^L$, and RNN acts as a bridge to traverse this distance, thereby informatively modeling the relation $x \to y$.

Figure 14 presents two stacking scenarios for $\mathcal{Y}$ within the $\{\mathcal{X}, \mathcal{Y}, \mathcal{Z}\}$ system, according to different causal directions. Given the established $\mathcal{X} \to \mathcal{Y}$ relationship in $\mathbb{R}^L$, the left-side architecture completes $\mathcal{X} \to \mathcal{Y} \leftarrow \mathcal{Z}$ structure, while the right-side caters to $\mathcal{X} \to \mathcal{Y} \to \mathcal{Z}$. By stacking an additional representation layer, hierarchical disentanglement is formed, allowing for various input-output combinations (denoted as $\mapsto$) based on practical needs. For instance, in the left-side setup, $\mathbf{P}(v|h) \mapsto \mathbf{P}(\alpha)$ signifies the $\mathcal{X} \to \mathcal{Y}$ relationship, while $\mathbf{P}(\alpha|k)$ suggests $\mathcal{Z} \to \mathcal{Y}$. On the right side, $\mathbf{P}(v) \mapsto P(\beta|k)$ indicates the $\mathcal{Y} \to \mathcal{Z}$ relationship with $\mathcal{Y}$ as input; conversely, $\mathbf{P}(v|h) \mapsto P(\beta|k)$ signifies the causal chain $\mathcal{X} \to \mathcal{Y} \to \mathcal{Z}$.

[1] https://github.com/kflijia/bijective_crossing_functions/blob/main/code_bicross_extracter.py

Causal relationships of known edges can be sequentially stacked using existing causal DAGs in domain knowledge. Additionally, this approach aids in discovering causal structures within the latent space by identifying potential relationships among the initial variable representations.

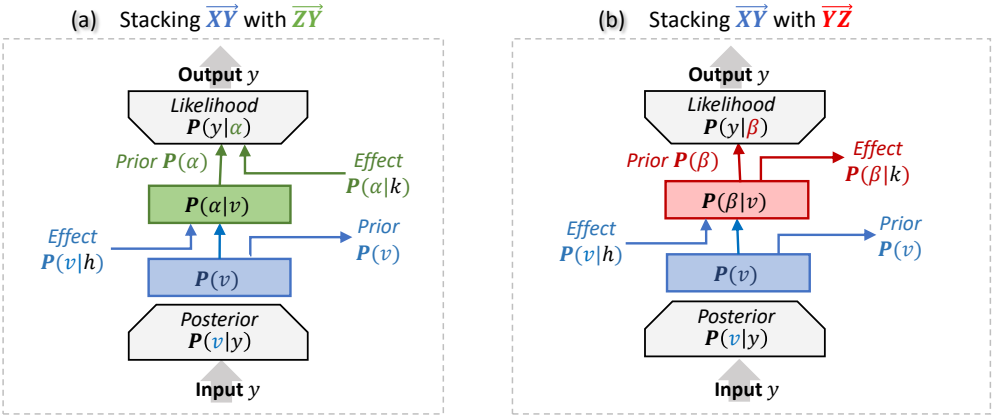

Figure 14: Architecutres of the relation-defined hierarchical disentanglement.

6.3 Causal Discovery in Latent Space

Algorithm 1 outlines the heuristic procedure for identifying edges among the initial variable representations. We use Kullback-Leibler Divergence (KLD) as a metric to evaluate the strength of causal relationships. Specifically, as depicted in Figure 13, KLD evaluates the similarity between the RNN output $\mathbf{P}(v|h)$ and the prior $\mathbf{P}(v)$. Lower KLD values indicate stronger causal relationships due to closer alignment with the ground truth. Although Mean Squared Error (MSE) is a common evaluation metric, its susceptibility to data variances Reisach et al. (2021); Kaiser & Sipos (2021) led us to prefer KLD, using MSE as a secondary measure. In the graphical representation context, we refer to variables A and B in the edge $A \rightarrow B$ as the *cause node* and *result node*, respectively.

Algorithm 1: Latent Space Causal Discovery

Result: ordered edges set $\mathbf{E} = \{e_1, \ldots, e_n\}$
$\mathbf{E} = \{\}$; $N_R = \{n_0 \mid n_0 \in N, Parent(n_0) = \varnothing\}$;
while $N_R \subset N$ **do**
  $\Delta = \{\}$;
  for $n \in N$ **do**
    for $p \in Parent(n)$ **do**
      if $n \notin N_R$ *and* $p \in N_R$ **then**
        $e = (p, n)$; $\beta = \{\}$;
        for $r \in N_R$ **do**
          if $r \in Parent(n)$ *and* $r \neq p$ **then**
            $\beta = \beta \cup r$
          end
        end
        $\delta_e = K(\beta \cup p, n) - K(\beta, n)$;
        $\Delta = \Delta \cup \delta_e$;
      end
    end
  end
  $\sigma = argmin_e(\delta_e \mid \delta_e \in \Delta)$;
  $\mathbf{E} = \mathbf{E} \cup \sigma$; $N_R = N_R \cup n_\sigma$;
end

$G = (N, E)$	graph G consists of N and E
N	the set of nodes
E	the set of edges
N_R	the set of reachable nodes
$\mathbf{E}$	the list of discovered edges
$K(\beta, n)$	KLD metric of effect $\beta \rightarrow n$
β	the cause nodes
n	the result node
δ_e	KLD Gain of candidate edge e
$\Delta = \{\delta_e\}$	the set $\{\delta_e\}$ for e
n,p,r	notations of nodes
e,σ	notations of edges

Figure 15 illustrates the causal structure discovery process in latent space over four steps. Two edges, (e_1 and e_3), are sequentially selected, with e_1 setting node B as the starting point for e_3. In step 3, edge e_2 from A to C is deselected and reassessed due to the new edge e_3 altering C's existing causal conditions. The final DAG represents the resulting causal structure.

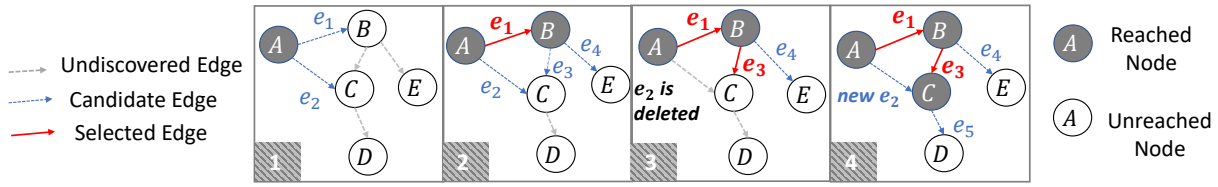

Figure 15: An example of causal discovery in the latent space.

7 Efficacy Validation Experiments

The experiments aim to validate the efficacy of the *relation-defined representation* learning method in three areas: 1) extracting higher-dimensional representations with the proposed autoencoder architecture, 2) hierarchically establishing relation-defined representations, and 3) discovering DAG structure in latent space. A full demonstration of the experiments conducted in this study is available online [2].

We use a synthetic hydrology dataset for our experiments, a common resource in the field of hydrology. The task focuses on predicting streamflow based on observed environmental conditions like temperature and precipitation. The application of relation-defined representation learning aims to create a streamflow prediction model that is generalizable across various watersheds. While these watersheds share a fundamental hydrological scheme governed by physical rules, they may exhibit unique features due to unobserved conditions such as economic development and land use. Current models based on physical knowledge, however, often lack the flexibility to fully capture multiple levels of dynamical temporal features across these watersheds.

In fact, to evaluate model robustness and generalizability, health informatics data would be optimal due to their complex confounding dynamics across multiple timelines. However, empirical constraints prevented us from accessing such data for this study. For insights into inherent temporal bias, we refer readers to previous work Li et al. (2020).

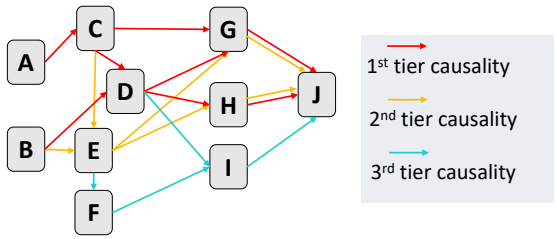

ID	Variable Name	Explanation
A	Environmental set I	Wind Speed, Humidity, Temperature
B	Environmental set II	Temperature, Solar Radiation, Precipitation
C	Evapotranspiration	Evaporation and transpiration
D	Snowpack	The winter frozen water in the ice form
E	Soil Water	Soil moisture in vadose zone
F	Aquifer	Groundwater storage
G	Surface Runoff	Flowing water over the land surface
H	Lateral	Vadose zone flow
I	Baseflow	Groundwater discharge
J	Streamflow	Sensors recorded outputs

Figure 16: Hydrological causal DAG: routine tiers organized by descending causal strength.

7.1 Hydrology Dataset

In hydrology, deep learning, particularly RNN models, has gained favor for extracting observational representations and predicting streamflow Goodwell et al. (2020); Kratzert (2018). For our experiments, we employ the Soil and Water Assessment Tool (SWAT), a comprehensive system grounded in physical modules, to generate dynamically significant hydrological time series. We focus on a simulation of the Root River Headwater watershed in Southeast Minnesota, covering 60 consecutive virtual years with daily updates.

Figure 16 displays the causal DAG employed by SWAT, complete with node descriptions. The hierarchy of hydrological routines is color-coded based on their contribution to output streamflow. Surface runoff (1st tier) significantly impacts rapid streamflow peaks, followed by lateral flow (2nd tier). Baseflow dynamics (3rd tier) have a subtler influence. Our causal discovery experiments aim to reveal these underlying relationships from the observed data.

[2] https://github.com/kflijia/bijective_crossing_functions.git

Table 1: Statistics of variable attributes and performances of the variable representation test.

Variable	Dim	Mean	Std	Min	Max	Non-Zero Rate%	RMSE on Scaled	RMSE on Unscaled	BCE of Mask
A	5	1.8513	1.5496	-3.3557	7.6809	87.54	0.093	0.871	0.095
B	4	0.7687	1.1353	-3.3557	5.9710	64.52	0.076	0.678	1.132
C	2	1.0342	1.0025	0.0	6.2145	94.42	0.037	0.089	0.428
D	3	0.0458	0.2005	0.0	5.2434	11.40	0.015	0.679	0.445
E	2	3.1449	1.0000	0.0285	5.0916	100	0.058	3.343	0.643
F	4	0.3922	0.8962	0.0	8.6122	59.08	0.326	7.178	2.045
G	4	0.7180	1.1064	0.0	8.2551	47.87	0.045	0.81	1.327
H	4	0.7344	1.0193	0.0	7.6350	49.93	0.045	0.009	1.345
I	3	0.1432	0.6137	0.0	8.3880	21.66	0.035	0.009	1.672
J	1	0.0410	0.2000	0.0	7.8903	21.75	0.007	0.098	1.088

Table 2: Brief summary of the latent space causal discovery test.

Edge	A→C	B→D	C→D	C→G	D→G	G→J	D→H	H→J	B→E	E→G	E→H	C→E	E→F	F→I	I→J	D→I
KLD	7.63	8.51	10.14	11.60	27.87	5.29	25.19	15.93	37.07	39.13	39.88	46.58	53.68	45.64	17.41	75.57
Gain	7.63	8.51	1.135	11.60	2.454	5.29	25.19	0.209	37.07	-5.91	-3.29	2.677	53.68	45.64	0.028	3.384

7.2 Higher-Dimensional Variable Representation Test

In this test, we have a total of ten variables (or nodes), each requiring a separate autoencoder for initializing a higher-dimensional representation. Table 1 lists the statistics of their post-scaled (i.e., normalized) attributes, as well as their autoencoders' reconstruction accuracies. Accuracy is assessed in the root mean square error (RMSE), where a lower RMSE indicates higher accuracy for both scaled and unscaled data.

The task is challenging due to the limited dimensionality of the ten variables - maxing out at just 5 dimensions and the target node, J, having just one attribute. To mitigate this, we duplicate their columns to a consistent 12 dimensions and add 12 dummy variables for months, resulting in a 24-dimensional input. A double-wise extension amplifies this to 576 dimensions, from which a 16-dimensional representation is extracted via the autoencoder. Another issue is the presence of meaningful zero-values, such as node D (Snowpack in winter), which contributes numerous zeros in other seasons and is closely linked to node E (Soil Water). We tackle this by adding non-zero indicator variables, called *masks*, evaluated via binary cross-entropy (BCE).

Despite challenges, RMSE values ranging from 0.01 to 0.09 indicate success, except for node F (the Aquifer). Given that aquifer research is still emerging (i.e., the 3rd tier baseflow routine), it is likely that node F in this synthetic dataset may better represent noise than meaningful data.

7.3 Hierarchical Relation-Defined Representations Test

Table 3 presents the results of the relation-defined representation learning. We use the term "single-effect" to describe the accuracy of a specific result node when reconstructed from a single cause node (e.g., $B \rightarrow D$ and $C \rightarrow D$), and "full-effect" for the accuracy when all its cause nodes are stacked (e.g., $BC \rightarrow D$). To provide context, we also include baseline performance scores based on the initial variable representations. During the relation learning process, the result node serves two purposes: it maintains its own accurate representation (as per optimization no.2 in 6.2) and helps reconstruct the relationship (as per optimization no.1). Both aspects are evaluated in Table 3.

The KLD metrics in Table 3 indicate the strength of learned causality, with a lower value signifying stronger. For instance, node J's minimal KLD values suggest a significant effect caused by nodes G (Surface Runoff), H (Lateral), and I (Baseflow). In contrast, the high KLD values imply that predicting variable I using D and F is challenging. For nodes D, E, and J, the "full-effect" are moderate compared to their "single-effect" scores, suggesting a lack of informative associations among the cause nodes. In contrast, for nodes G and H, lower "full-effect" KLD values imply capturing meaningful associative effects through hierarchical stacking. The KLD metric also reveals the most contributive cause node to the result node. For example, the proximity of the $C \rightarrow G$ strength to $CDE \rightarrow G$ suggests that C is the primary contributor to this causal relationship.

Figure 17 showcases reconstructed time series, for the result nodes J, G, and I, in the same synthetic year to provide a straightforward overview of the hierarchical representation performances. Here, black dots represent the ground truth; the blue line indicates reconstruction via the initial variable representation, and the "full-effect" representation generates the red line. In addition to RMSE, we also employ the Nash–Sutcliffe

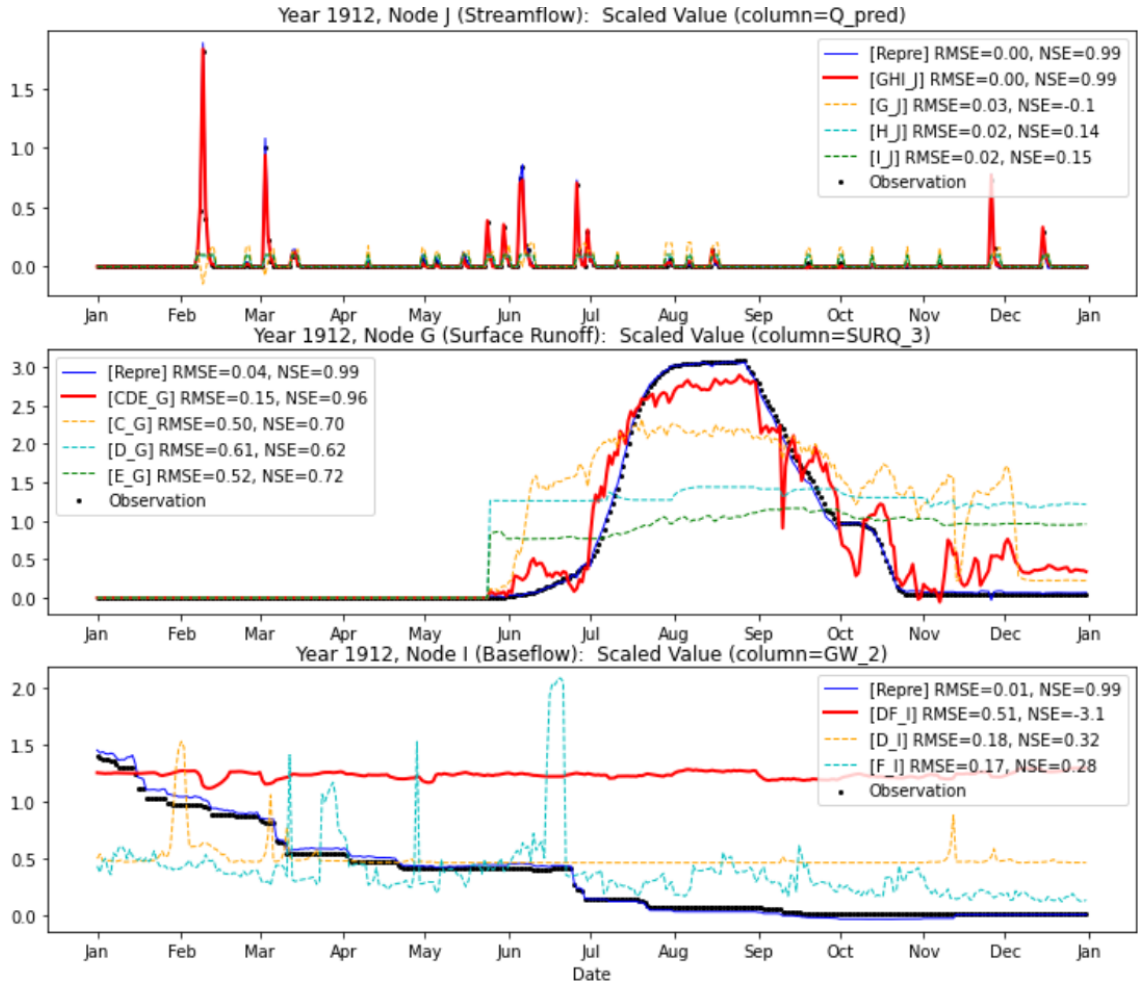

Figure 17: Reconstructed time series, via hierarchically stacked relation-defined representations.

model efficiency coefficient (NSE) as an accuracy metric, commonly used in hydrological predictions. The NSE ranges from -∞ to 1, with values closer to 1 indicating higher accuracy.

The initial variable representation closely aligns with the ground truth, as shown in Figure 17, attesting to the efficacy of our proposed autoencoder architecture. As expected, the "full-effect" performs better than the "single-effect" for each result node. Node J exhibits the best prediction, whereas node I presents a challenge. For node G, causality from C proves to be significantly stronger than the other two, D and E.

One may observe via the demo that our experiments do not show smooth information flows along successive long causal chains. Since RNNs are designed primarily for capturing the dynamics of causes rather than the effects, relying on them to autonomously construct dynamical representations of the effects might prove unreliable. It underscores a significant opportunity for enhancing effectiveness by improving the architecture.

7.4 Latent Space Causal Discovery Test

The discovery test initiates with source nodes A and B and proceeds to identify potential edges, culminating in the target node J. Candidate edges are selected based on their contributions to the overall KLD sum (less gain is better). Table 6 shows the order in which existing edges are discovered, along with the corresponding KLD sums and gains after each edge is included. Color-coding in the cells corresponds to Figure 16, indicating tiers of causal routines. The arrangement underscores the efficacy of this latent space discovery approach.

A comprehensive list of candidate edges evaluated in each discovery round is provided in Table 4 in Appendix A. For comparative purposes, we also performed a 10-fold cross-validation using the conventional FGES discovery method; those results are available in Table 5 in Appendix A.

Table 3: Performances of the relation-defined representations, sorted by the result node.

Result Node	Variable Representation (Initial)			Cause Node	Variable Representation (in Relation Learning)			Relationship Reconstruction			
	RMSE		BCE		RMSE		BCE	RMSE		BCE	KLD
	on Scaled Values	on Unscaled Values	Mask		on Scaled Values	on Unscaled Values	Mask	on Scaled Values	on Unscaled Values	Mask	(in latent space)
C	0.037	0.089	0.428	A	0.0295	0.0616	0.4278	0.1747	0.3334	0.4278	7.6353
D	0.015	0.679	0.445	BC	0.0350	1.0179	0.1355	0.0509	1.7059	0.1285	9.6502
				B	0.0341	1.0361	0.1693	0.0516	1.7737	0.1925	8.5147
				C	0.0331	0.9818	0.3404	0.0512	1.7265	0.3667	10.149
E	0.058	3.343	0.643	BC	0.4612	26.605	0.6427	0.7827	45.149	0.6427	39.750
				B	0.6428	37.076	0.6427	0.8209	47.353	0.6427	37.072
				C	0.5212	30.065	1.2854	0.7939	45.791	1.2854	46.587
F	0.326	7.178	2.045	E	0.4334	8.3807	3.0895	0.4509	5.9553	3.0895	53.680
G	0.045	0.81	1.327	CDE	0.0538	0.9598	0.0878	0.1719	3.5736	0.1340	8.1360
				C	0.1057	1.4219	0.1078	0.2996	4.6278	0.1362	11.601
				D	0.1773	3.6083	0.1842	0.4112	8.0841	0.2228	27.879
				E	0.1949	4.7124	0.1482	0.5564	10.852	0.1877	39.133
H	0.045	0.009	1.345	DE	0.0889	0.0099	2.5980	0.3564	0.0096	2.5980	21.905
				D	0.0878	0.0104	0.0911	0.4301	0.0095	0.0911	25.198
				E	0.1162	0.0105	0.1482	0.5168	0.0097	3.8514	39.886
I	0.035	0.009	1.672	DF	0.0600	0.0103	3.4493	0.1158	0.0099	3.4493	49.033
				D	0.1212	0.0108	3.0048	0.2073	0.0108	3.0048	75.577
				F	0.0540	0.0102	3.4493	0.0948	0.0098	3.4493	45.648
J	0.007	0.098	1.088	GHI	0.0052	0.0742	0.2593	0.0090	0.1269	0.2937	5.5300
				G	0.0077	0.1085	0.4009	0.0099	0.1390	0.4375	5.2924
				H	0.0159	0.2239	0.4584	0.0393	0.5520	0.4938	15.930
				I	0.0308	0.4328	0.3818	0.0397	0.5564	0.3954	17.410

8 Conclusions

Motivated by the issue of AI misalignment, we explore the inherent limitation of the prevalent *Observation-Oriented* paradigm and introduce a new *Relation-Oriented* one, complemented by the practical approach of *relation-defined representation* learning, and validate its efficacy through experimentations.

This research introduces a dimensionality framework for understanding relationship learning, offering new, intuitive insights into causal inference and highlighting the restrictions of the existing *Observation-Oriented* paradigm. This paradigm typically requires pre-identification of modeling objects before defining relations, which confines models to the *observational* space, limiting their access to dynamical temporal features. Further, by relying on a single, absolute timeline, it neglects the multi-dimensional nature of the *temporal* feature space, compromising both model robustness and generalizability.

At its core, human cognition prioritizes relations, giving rise to our vast relation-centric knowledge systems. We can identify dynamics by navigating the intricate network of relations in unobservable *hyper-dimensional* space. This insight inspired the *Relation-Oriented* paradigm.

While implementing relation-defined representation learning, we faced significant challenges, including designing an invertible autoencoder for higher-dimensional representation. Nevertheless, thorough experiments have affirmed the feasibility of the proposed methodology. AI alignment is never a question with a simple answer but calls for interdisciplinary efforts Christian (2020). Through this work, we aim to contribute to developing more genuine AI and provide a foundation for future advancements.

References

Howard Alkon, Daniel L & Rasmussen. A spatial-temporal model of cell activation. *Science*, 239(4843): 998–1005, 1988.

Gennady & Gatalsky Peter Andrienko, Natalia & Andrienko. Exploratory spatio-temporal visualization: an analytical review. *Journal of Visual Languages & Computing*, 14(6):503–541, 2003.

Pierre Baldi and Kurt Hornik. Neural networks and principal component analysis: Learning from examples without local minima. *Neural networks*, 2(1):53–58, 1989.

Brian Christian. *The alignment problem: Machine learning and human values.* 2020.

A Philip Dawid. Conditional independence in statistical theory. *Journal of the Royal Statistical Society: Series B (Methodological)*, 41(1):1–15, 1979.

Laurent Dinh, Jascha Sohl, and Samy Bengio. Density estimation using real nvp. *arXiv:1605.08803*, 2016.

Felix Elwert. Graphical causal models. *Handbook of causal analysis for social research*, pp. 245–273, 2013.

Dan Geiger and Judea Pearl. Logical and algorithmic properties of conditional independence and graphical models. *The annals of statistics*, 21(4):2001–2021, 1993.

Clark Glymour, Kun Zhang, and Peter Spirtes. Review of causal discovery methods based on graphical models. *Frontiers in genetics*, 10:524, 2019.

Allison E Goodwell, Peishi Jiang, Benjamin L Ruddell, and Praveen Kumar. Debates—does information theory provide a new paradigm for earth science? causality, interaction, and feedback. *Water Resources Research*, 56(2):e2019WR024940, 2020.

Yimin Huang and Marco Valtorta. Pearl's calculus of intervention is complete. *arXiv preprint arXiv:1206.6831*, 2012.

Aapo Hyvärinen, Kun Zhang, Shohei Shimizu, and Patrik O Hoyer. Estimation of a structural vector autoregression model using non-gaussianity. *Journal of Machine Learning Research*, 11(5), 2010.

Saachi Jain, Adityanarayanan Radhakrishnan, and Caroline Uhler. A mechanism for producing aligned latent spaces with autoencoders. *arXiv preprint arXiv:2106.15456*, 2021.

Marcus Kaiser and Maksim Sipos. Unsuitability of notears for causal graph discovery. *arXiv:2104.05441*, 2021.

Frederik et. al Kratzert. Rainfall–runoff modelling using lstm networks. *Hydrology and Earth System Sciences*, 22(11):6005–6022, 2018.

Sébastien Lachapelle, Philippe Brouillard, Tristan Deleu, and Simon Lacoste-Julien. Gradient-based neural dag learning. *arXiv preprint arXiv:1906.02226*, 2019.

Jia Li, Xiaowei Jia, Haoyu Yang, Vipin Kumar, Michael Steinbach, and Gyorgy Simon. Teaching deep learning causal effects improves predictive performance. *arXiv preprint arXiv:2011.05466*, 2020.

Yunan Luo, Jian Peng, and Jianzhu Ma. When causal inference meets deep learning. *Nature Machine Intelligence*, 2(8):426–427, 2020.

Jianzhu et. al Ma. Using deep learning to model the hierarchical structure and function of a cell. *Nature methods*, 15(4):290–298, 2018.

Mariusz Maziarz. A review of the granger-causality fallacy. *The journal of philosophical economics: Reflections on economic and social issues*, 8(2):86–105, 2015.

Mohammed Ombadi, Phu Nguyen, Soroosh Sorooshian, and Kuo-lin Hsu. Evaluation of methods for causal discovery in hydrometeorological systems. *Water Resources Research*, 56(7):e2020WR027251, 2020.

Judea Pearl. Causal inference in statistics: An overview. 2009.

Judea Pearl. The do-calculus revisited. *arXiv preprint arXiv:1210.4852*, 2012.

Judea Pearl et al. Models, reasoning and inference. *Cambridge, UK: CambridgeUniversityPress*, 19(2), 2000.

Jonas Peters, Joris M Mooij, Dominik Janzing, and Bernhard Schölkopf. Causal discovery with continuous additive noise models. 2014.

Jonas Peters, Dominik Janzing, and Bernhard Scholkopf. *Elements of causal inference: foundations and learning algorithms*. The MIT Press, 2017.

David Pitt. Mental Representation. In Edward N. Zalta and Uri Nodelman (eds.), *The Stanford Encyclopedia of Philosophy*. Metaphysics Research Lab, Stanford University, Fall 2022 edition, 2022.

Elad Plaut. From principal subspaces to principal components with linear autoencoders. *arXiv:1804.10253*, 2018.

Alexander G Reisach, Christof Seiler, and Sebastian Weichwald. Beware of the simulated dag! varsortability in additive noise models. *arXiv preprint arXiv:2102.13647*, 2021.

Richard Scheines. An introduction to causal inference. 1997.

Bernhard Scholkopf, Francesco Locatello, Stefan Bauer, Nan Rosemary Ke, Nal Kalchbrenner, Anirudh Goyal, and Yoshua Bengio. Toward causal representation learning. *IEEE*, 109(5):612–634, 2021.

Richard S Sutton and Andrew G Barto. *Reinforcement learning: An introduction*. MIT press, 2018.

Monica G Turner. Spatial and temporal analysis of landscape patterns. *Landscape ecology*, 4:21–30, 1990.

Stefan Vuković, Matej & Thalmann. Causal discovery in manufacturing: A structured literature review. *Journal of Manufacturing and Materials Processing*, 6(1):10, 2022.

Yasi Wang, Hongxun Yao, and Sicheng Zhao. Auto-encoder based dimensionality reduction. 184:232–242, 2016.

Robert W Wood, Christopher J & Spekkens. The lesson of causal discovery algorithms for quantum correlations: Causal explanations of bell-inequality violations require fine-tuning. *New Journal of Physics*, 17 (3):033002, 2015.

Haoyan Xu, Yida Huang, Ziheng Duan, Jie Feng, and Pengyu Song. Multivariate time series forecasting based on causal inference with transfer entropy and graph neural network. *arXiv:2005.01185*, 2020.

Xun Zheng, Bryon Aragam, Pradeep K Ravikumar, and Eric P Xing. Dags with no tears: Continuous optimization for structure learning. *Advances in neural information processing systems*, 31, 2018.

Xun Zheng, Chen Dan, Bryon Aragam, Pradeep Ravikumar, and Eric Xing. Learning sparse nonparametric dags. In *International Conference on Artificial Intelligence and Statistics*, pp. 3414–3425. PMLR, 2020.

A Appendix: Complete Experimental Results of Causal Discovery

Table 4: The Complete Results of Heuristic Causal Discovery in latent space. Each row stands for a round of detection, with '#" identifying the round number, and all candidate edges are listed with their KLD gains as below. 1) Green cells: the newly detected edges. 2) Red cells: the selected edge. 3) Blue cells: the trimmed edges accordingly.

# 1	**A→ C**	A→ D	A→ E	A→ F	**B→ C**	B→ D	B→ E	B→ F								
	7.6354	19.7407	60.1876	119.7730	**8.4753**	8.5147	65.9335	132.7717								
# 2	A→ D	A→ E	A→ F	**B→ D**	B→ E	B→ F	C→ D	C→ E	C→ F	C→ G	C→ H	C→ I				
	19.7407	60.1876	119.7730	**8.5147**	65.9335	132.7717	10.1490	46.5876	111.2978	11.6012	39.2361	95.1564				
# 3	**A→ D**	A→ E	A→ F	B→ E	B→ F	**C→ D**	C→ E	C→ F	C→ G	C→ H	C→ I	D→ E	D→ F	D→ G	D→ H	D→ I
	9.7357	60.1876	119.7730	65.9335	132.7717	**1.1355**	46.5876	111.2978	11.6012	39.2361	95.1564	63.7348	123.3203	27.8798	25.1988	75.5775
# 4	A→ E	A→ F	B→ E	B→ F	C→ E	C→ F	**C→ G**	C→ H	C→ I	D→ E	D→ F	D→ G	D→ H	D→ I		
	60.1876	119.7730	65.9335	132.7717	46.5876	111.2978	**11.6012**	39.2361	95.1564	63.7348	123.3203	27.8798	25.1988	75.5775		
# 5	A→ E	A→ F	B→ E	B→ F	C→ E	C→ F	C→ H	C→ I	D→ E	D→ F	**D→ G**	D→ H	D→ I	G→ J		
	60.1876	119.7730	65.9335	132.7717	46.5876	111.2978	39.2361	95.1564	63.7348	123.3203	**2.4540**	25.1988	75.5775	5.2924		
# 6	A→ E	A→ F	B→ E	B→ F	C→ E	C→ F	C→ H	C→ I	D→ E	D→ F	D→ H	D→ I	**G→ J**			
	60.1876	119.7730	65.9335	132.7717	46.5876	111.2978	39.2361	95.1564	63.7348	123.3203	25.1988	75.5775	**5.2924**			
# 7	A→ E	A→ F	B→ E	B→ F	C→ E	C→ F	**C→ H**	C→ I	D→ E	D→ F	**D→ H**	D→ I				
	60.1876	119.7730	65.9335	132.7717	46.5876	111.2978	**39.2361**	95.1564	63.7348	123.3203	**25.1988**	75.5775				
# 8	A→ E	A→ F	B→ E	B→ F	C→ E	C→ F	C→ I	D→ E	D→ F	D→ I	**H→ J**					
	60.1876	119.7730	65.9335	132.7717	46.5876	111.2978	95.1564	63.7348	123.3203	75.5775	**0.2092**					
# 9	**A→ E**	A→ F	B→ E	B→ F	**C→ E**	C→ F	C→ I	D→ E	D→ F	D→ I						
	60.1876	119.7730	65.9335	132.7717	**46.5876**	111.2978	95.1564	63.7348	123.3203	75.5775						
# 10	A→ F	B→ E	B→ F	C→ F	C→ I	**D→ E**	D→ F	D→ I	E→ F	E→ G	E→ H	E→ I				
	119.7730	**-6.8372**	132.7717	111.2978	95.1564	**17.0407**	123.3203	75.5775	53.6806	-5.9191	-3.2931	110.2558				
# 11	A→ F	B→ F	C→ F	C→ I	D→ F	D→ I	E→ F	**E→ G**	E→ H	E→ I						
	119.7730	132.7717	111.2978	95.1564	123.3203	75.5775	53.6806	**-5.9191**	-3.2931	110.2558						
# 12	A→ F	B→ F	C→ F	C→ I	D→ F	D→ I	E→ F	**E→ H**	E→ I							
	119.7730	132.7717	111.2978	95.1564	123.3203	75.5775	53.6806	**-3.2931**	110.2558							
# 13	**A→ F**	**B→ F**	**C→ F**	C→ I	**D→ F**	D→ I	**E→ F**	E→ I								
	119.7730	**132.7717**	**111.2978**	95.1564	**123.3203**	75.5775	**53.6806**	110.2558								
# 14	C→ I	D→ I	**E→ I**	**F→ I**												
	95.1564	75.5775	**110.2558**	**45.6490**												
# 15	C→ I	D→ I	**I→ J**													
	15.0222	3.3845	**0.0284**													
# 16	**C→ I**	**D→ I**														
	15.0222	**3.3845**														

Table 5: Average performance of 10-Fold FGES (Fast Greedy Equivalence Search) causal discovery, with the prior knowledge that each node can only cause the other nodes with the same or greater depth with it. An edge means connecting two attributes from two different nodes, respectively. Thus, the number of possible edges between two nodes is the multiplication of the numbers of their attributes, i.e., the lengths of their data vectors.
(All experiments are performed with 6 different Independent-Test kernels, including chi-square-test, d-sep-test, prob-test, disc-bic-test, fisher-z-test, mvplr-test. But their results turn out to be identical.)

Cause Node	A	B		C			D			E			F	G		H	I
True Causation	A→ C	B→ D	B→ E	C→ D	C→ E	C→ G	D→ G	D→ H	D→ I	E→ F	E→ G	E→ H	F→ I	G→ J		H→ J	I→ J
Number of Edges	16	24	16	6	4	8	12	12	9	8	8	8	12	4		4	3
Probability of Missing	0.038889	0.125	0.125	0.062	0.06875	0.039286	0.069048	0.2	0.142857	0.3	0.003571	0.2	0.142857	0.0		0.072727	0.030303
Wrong Causation				C→ F				D→ E	D→ F				F→ G	G→ H	G→ I	H→ I	
Times of Wrongly Discovered				5.6				1.2	0.8				5.0	8.2	3.0	2.8	

Table 6: Brief Results of the Heuristic Causal Discovery in latent space, identical with Table 3 in the paper body, for better comparison to the traditional FGES methods results on this page.
The edges are arranged in detected order (from left to right) and their measured causal strengths in each step are shown below correspondingly. Causal strength is measured by KLD values (less is stronger). Each round of detection is pursuing the least KLD gain globally. All evaluations are in 4-Fold validation average values. Different colors represent the ground truth causality strength tiers (referred to the Figure 10 in the paper body).

Causation	A→ C	B→ D	C→ D	C→ G	D→ G	G→ J	D→ H	H→ J	C→ E	B→ E	E→ G	E→ H	E→ F	F→ I	I→ J	D→ I
KLD	7.63	8.51	10.14	11.60	27.87	5.29	25.19	15.93	46.58	65.93	39.13	39.88	53.68	45.64	17.41	75.57
Gain	7.63	8.51	1.135	11.60	2.454	5.29	25.19	0.209	46.58	-6.84	-5.91	-3.29	53.68	45.64	0.028	3.384